THE CLOUDY LIFE OF THE GALACTIC CENTER

ROMAN V. SHCHERBAKOV[1,2,3]

Draft version September 11, 2013

ABSTRACT

The object G2 was recently discovered descending deep into the gravitational potential of the supermassive black hole (BH) Sgr A*. We test the photoionized cloud scenario for the object, determine the cloud properties, and estimate the emission during the pericenter passage. The incident radiation is computed starting from the individual stars at the locations of G2 in different years. The radiative transfer calculations are conducted with CLOUDY code and the 2011 luminosities in Brγ line, HeI line, M band, and L' band are fitted. The spherically symmetric, tidally distorted, and magnetically arrested cloud shapes are tested with both the interstellar medium (ISM) dust and the 10 nm graphite dust. The best-fitting magnetically arrested cloud model has the density $n_{\rm init} = 3.6 \times 10^4 \rm cm^{-3}$, the radius $R_{\rm init} = 5.5 \times 10^{15} \rm cm = 43 mas$, and the dust relative abundance $A = 0.65$. It provides an excellent fit to the 2011 data, is consistent with the luminosities in 2004 and 2008, and reaches an agreement with the velocity spread. The bow shock is estimated to pass the pericenter in 2012 about $\Delta t \approx 1.8$ yrs before the center of mass (CM). The radio luminosity comparable to the quiescent level of Sgr A* and the X-ray synchrotron luminosity several times the quiescent level are achieved by the bow shock in the best-fitting model. The magnetic energy dissipation as the CM reaches the pericenter may lead, depending on the dissipation rate, to a relatively bright infrared source with the apparent magnitudes up to $m_M \approx 13.0$, $m_{L'} \approx 13.0$, and $m_{Ks} \approx 14.6$. Larger than previously estimated cloud mass $m_{\rm cloud} = 13 M_{\rm Earth}$ may produce a higher accretion rate and a brighter state of Sgr A* as the cloud debris descend onto the BH.

Subject headings: black hole physics — Galaxy: center — ISM: clouds — magnetic fields — radiation mechanisms: general — radiative transfer

1. INTRODUCTION

The center of our Milky Way galaxy hosts a supermassive black hole (BH) Sgr A* with a mass $M_{\rm BH} = 4.3 \times 10^6 M_\odot$ located at a distance $d = 8.3$ kpc (Ghez et al. 2008; Gillessen et al. 2009b). The BH is primarily fed by hot stellar winds in the present epoch (Cuadra et al. 2008; Shcherbakov & Baganoff 2010), while clumps of cold gas provide an additional fuel source. The accretion of such clumps may have been responsible for multiple Sgr A* outbursts observed as light echoes (Clavel et al. 2013; Czerny et al. 2013). Another object first identified as a gas cloud G2 is observed on its way towards Sgr A* (Gillessen et al. 2012, 2013a). Its tail was later hypothesized to be unrelated to the cloud, so that the compact object scenario is not excluded (Phifer et al. 2013). G2 is on a deeply plunging orbit with the pericenter distance in the range $r_p = 1900 - 3100 r_S$ (Phifer et al. 2013; Gillessen et al. 2013b), where $r_S = 2GM_{\rm BH}/c^2$ is the Schwarzschild radius. The center of mass (CM) of the cloud is predicted to pass the pericenter in 2013 or 2014.

The G2 cloud may have formed from the colliding stellar winds, which are subject to runaway cooling in the densest regions(Cuadra et al. 2005, 2008). The other cloud formation scenarios are a creation of a protoplanetary disk (Murray-Clay & Loeb 2012), an encounter of a star with a stellar mass BH (Miralda-Escudé 2012), and a nova outburst (Meyer & Meyer-Hofmeister 2012). In all these cases the observed radiation comes from the gas photoionized and the dust heated by the intense starlight. Alternatively, the object could host a central young star, which expels stellar wind (Scoville & Burkert 2013). The winds encounter ambient medium and produce a reverse shock. The observed emission then comes from the collisionally ionized shocked gas.

The object was extensively studied in the infrared (IR) band. The intrinsic luminosities of Brackett-γ (Brγ), Paschen-α (Paα), and Helium-I (HeI) lines were determined to yield $L(\rm Br\gamma) = (1.06 \pm 0.32) 10^{31} \rm erg \, s^{-1}$ and the dereddened ratios $L(\rm Pa\alpha)/L(\rm Br\gamma) = 11.0 \pm 0.5$ and $L(\rm He$I$)/L(\rm Br\gamma) = 0.8 \pm 0.3$ in the year 2011 (Gillessen et al. 2013b). The luminosities of these three lines are consistent with constants: of Brγ from 2004 till 2012 and of the other two lines from 2008 till 2011. A constant $L(\rm Br\gamma)$ is not generally expected for a photoionized cloud (Scoville & Burkert 2013). The object was detected in L' and M bands with the dereddened absolute magnitudes $M_{L'} = -1.3 \pm 0.3$ and $M_M = -1.8 \pm 0.3$ in 2011. An upper limit with an apparent magnitude $m_{Ks} > (17 - 19)$ mag was measured in a Ks band in 2011 (Gillessen et al. 2012) and with $m_{Ks} \gtrsim 20$ mag in 2012 (Phifer et al. 2013). The latter limit is uncertain due to the source confusion (Gillessen et al. 2013b).

The observational manifestations of G2 passing close to Sgr A* were quantified. The bow shock during the pericenter passage accelerates a substantial amount of electrons. Correspondent synchrotron radiation leads to an observable flux increase in the radio band (Narayan et al. 2012; Sądowski et al. 2013). The radio flux predictions depend on the dynamics of the infall, in particular, on the cloud cross-section. If G2 is a cloud, then it is tidally disrupted at the pericenter (Gillessen et al. 2012). After the disruption some debris fall back onto Sgr A*, which leads to a higher accretion rate and higher quiescent luminosity (Mościbrodzka et al. 2012). The peak accretion rate and the duration of this state depend on the geometry and the

roman@astro.umd.edu
[1] http://astroman.org
Department of Astronomy, University of Maryland, College Park, MD 20742, USA
[2] Joint Space Science Institute, University of Maryland, College Park MD 20742, USA
[3] Hubble Fellow

cloud mass. Thus, knowing the cloud properties is important for predicting the observational manifestations. The cloud radius was observed to be $R_{cloud} \sim 15$ mas, which leads to the density $n_{cloud} = 2.6 \times 10^5 cm^{-3}$ and the mass $m_{cloud} = 3 M_{Earth}$ (Gillessen et al. 2012). These estimates are based on a simple photoionization of a spherical shape. A full radiative transfer calculation and fitting of the full IR dataset were not conducted. Neither the consistency of the cloud hypothesis with the temporal behavior of the observed emission was quantitatively addressed. The detailed emission diagnostics may either indicate that G2 is inconsistent with a gas cloud or confirm the cloud hypothesis and help to reliably determine the object properties.

In the present paper we perform such detailed analysis of G2 assuming a gas cloud paradigm. We compute the incident continuum from a set of massive stars with known coordinates and luminosities. We employ the radiative transfer code CLOUDY (Ferland et al. 1998, 2013) to simulate the emission from the dust and the photoionized gas. In Section 2 we describe three models for the cloud shape: the spherical, tidally distorted, and magnetically arrested. In Section 3 we present fitting of the simulated emission to the data. We explore both the 10 nm graphite dust grains and the full distribution of grain sizes incorporated into the interstellar medium (ISM) dust model. We find good fits to 2011 IR data and reproduce the temporal behavior of the IR emission with both the spherical and magnetically arrested cloud shapes. In Section 4 we adopt the best-fitting magnetically arrested G2 model and estimate radiation during the pericenter passage. An IR source is produced, when dissipation of the magnetic energy heats the cloud. The radio luminosity of the bow shock is revised down to about the quiescent level of Sgr A* owing to the smaller cloud cross-section. The synchrotron X-ray luminosity of the bow shock can exceed the quiescent X-ray power of Sgr A*. In Section 5 we discuss the results. In the paper we report the observed apparent magnitudes in the AB system $m_\nu = -2.5\log_{10}(F_\nu) - 48.6$ (Oke 1974) and the dereddened absolute magnitudes M. Correspondingly, the extinction is added to the simulated apparent magnitudes, but not to the simulated absolute magnitudes. The extinction coefficients towards the Galactic Center are $A_{Ks} = 2.42$, $A_{L'} = 1.23$, and $A_M = 1.07$ (Fritz et al. 2011).

2. DYNAMICAL MODELS OF THE G2 CLOUD

2.1. Spherical Cloud

A sphere is the simplest shape. The spherical cloud is characterized by the radius R_{init} and the proton density n_{init}. The shape stays constant with time, which might not represent the physical behavior of a tenuous gas clump with weak self-gravity. However, the additional gravity of the enclosed star may help to preserve the cloud shape (Phifer et al. 2013).

2.2. Tidally Distorted Cloud

A tenuous object is tidally disrupted, when it passes within the tidal radius

$$r_T = R_{init} \left(\frac{M_{BH}}{m_{cloud}} \right)^{1/3} \qquad (1)$$

from the BH. The tidal radius is $r_T = 150$ arcsec for the G2 properties estimated in Gillessen et al. (2012), It is much larger than the semi-major axis $a_{sem} = (0.5 - 1)$ arcsec (Gillessen et al. 2013b), so that the cloud self-gravity can be neglected. We consider the parts of the cloud to move independently in the gravitational field of Sgr A*. On its way towards the center G2 is stretched along the direction of motion and compressed in the perpendicular direction just like a spherically symmetric accretion flow. We denote by r_{init} the distance to Sgr A*, where the cloud is formed and where the spherical shape is assumed. The cloud may have formed near the apocenter, where it spends most of the time during the orbit. The G2 apocenter is at $r_{apo} \approx 2a_{sem} \sim 1$ arcsec, so that we take the formation distance to be

$$r_{init} = 1 arcsec. \qquad (2)$$

The tidally distorted cloud is characterized by the initial radius R_{init} and the initial density n_{init}, similarly to the spherical model. The half-length of such a cloud is

$$L = R_{init} \left(\frac{r}{r_{init}} \right)^{-1/2}, \qquad (3)$$

the perpendicular size is

$$\rho = R_{init} \frac{r}{r_{init}}, \qquad (4)$$

and the density is

$$n = n_{init} \left(\frac{r}{r_{init}} \right)^{-3/2} \qquad (5)$$

at any distance r from Sgr A*. The tidally distorted shape is more suitable, than the spherical shape, for the cloud without the central source, but it assumes zero magnetic field.

2.3. Magnetically Arrested Cloud

A strong magnetic field alters the shape of the cloud. We denote by σ the ratio of the magnetic field energy density to the gas energy density in the cloud at the place of formation, such that

$$\frac{B_{init}^2}{8\pi} = \sigma 3 k_B n_{init} T_{cloud}, \qquad (6)$$

where the cloud temperature is approximately $T_{cloud} \sim 8 \times 10^3$ K (Gillessen et al. 2012). The magnetic flux conservation along the direction of motion

$$B_{init} R_{init}^2 = B_{||} \rho^2 \qquad (7)$$

leads to a substantial growth of the B-field and the correspondent magnetic forces as in the spherical magnetized accretion flow (Shvartsman 1971; Shcherbakov 2008). Two dominant forces acting on the cloud perpendicular to its orbital plane are the gravitational force

$$F_g = \frac{G M_{BH} m_{cloud} \rho}{r^3}, \qquad (8)$$

where the cloud mass is $m_{cloud} = (2R_{init})^3 m_p n_{init}$, and the magnetic force

$$F_{magn} = \frac{B_{||}^2}{8\pi} 4 L \rho. \qquad (9)$$

The hot ambient gas force F_{out} and the cloud gas force F_{in} can be comparable to the magnetic force at the formation distance, but are sub-dominant inwards as the magnetization of the cloud grows.

The parallel force balance is dominated by the rapidly growing gravitational force $F_{g,||} \propto L/r^3 \propto r^{-7/2}$, so that the

cloud is stretched in the parallel direction according to the equation (3) as in the tidally distorted model. Solving the perpendicular force balance

$$F_{\rm g} = F_{\rm magn} \tag{10}$$

we find the perpendicular radius

$$\rho = 38{\rm mas} \left(\frac{r}{\rm arcsec}\right)^{5/8} \left(\frac{r_{\rm init}}{\rm arcsec}\right)^{1/8} \sqrt{\frac{R_{\rm init}}{0.1{\rm arcsec}}} \sigma^{1/4}, \tag{11}$$

which depends weakly on both the initial cloud magnetization σ and the formation distance. The distance from Sgr A*, where the cloud becomes magnetically arrested is

$$r_{\rm crit} = 78{\rm mas} \left(\frac{r_{\rm init}}{\rm arcsec}\right)^{3} \left(\frac{R_{\rm init}}{0.1{\rm arcsec}}\right)^{-4/3} \sigma^{2/3}. \tag{12}$$

There the perpendicular cloud size switches from $\rho \propto r$ to $\rho \propto r^{5/8}$ behavior. The critical distance $r_{\rm crit}$ equals the formation distance $r_{\rm init} = 1$ arcsec for the initial magnetization

$$\sigma_x = \left(\frac{R_{\rm init}}{15{\rm mas}}\right)^{2}. \tag{13}$$

The density is

$$n = n_{\rm init} \left(\frac{r}{r_{\rm init}}\right)^{-3/4} \tag{14}$$

of the cloud, which forms magnetically arrested. The column density of such a cloud is practically constant with distance to Sgr A* as $n\rho \propto r^{1/8}$. We define the free-fall time at the distance r as

$$t_{\rm ff} = \frac{r}{v_K}, \quad \text{where} \quad v_K = \sqrt{\frac{GM_{\rm BH}}{r}} \tag{15}$$

is the Keplerian velocity. The efficient magnetic energy dissipation occurs on the Alfven timescale

$$t_{\rm A} = \frac{\rho}{v_{\rm A}}, \quad \text{where} \quad v_{\rm A} = \frac{B_{||}}{\sqrt{4\pi n m_p}} \tag{16}$$

is the Alfven speed. The ratio of these timescales is always

$$\frac{t_{\rm A}}{t_{\rm ff}} = \frac{1}{2} \tag{17}$$

in the magnetically arrested regime. Efficient energy dissipation happens over the dynamical time, and then the cloud shape approaches the tidally distorted shape. However, the continuous magnetic field dissipation during the formation and the initial motion of the cloud is likely to leave the large scale ordered magnetic field or the highly helical magnetic field (Biskamp 2003; Shcherbakov 2008). The resultant inefficient dissipation occurs on the large timescale

$$t_{\rm diss} \gg t_{\rm A}. \tag{18}$$

We adopt the latter case of the weak dissipation and neglect the influence of the finite $t_{\rm diss}$ on the cloud shape. We fit the 2011 observational data and explore the temporal behavior of the models for all three presented shapes.

3. EMISSION LINES AND DUST DIAGNOSTICS

3.1. *Incident Radiation*

The incident radiation flux and spectrum need to be reliably determined to model the cloud. We quantify the incident radiation starting from the properties of the individual bright stars in the Galactic Center region. We take the positions and the velocities of the bright stars from Paumard et al. (2006); Lu et al. (2009) and the stellar temperatures and luminosities from Martins et al. (2007). Following Cuadra et al. (2008) we correct the sample of Wolf-Rayet stars for completeness. The incident flux emitted by the bright stars is dominated at Sgr A* by IRS16NW, IRS16C, and IRS16SW. The vertical offset z of IRS16NW and IRS16C are not known, but their z velocities are much larger than that of IRS16SW (Lu et al. 2009). Then we assume IRS16NW and IRS16C to have zero vertical offsets $z = 0$. The rest of the bright stars contribute about $1/3$ of the total flux from these three. The IRS16 stars are more than 1 arcsec away from Sgr A*. The closer in, but less luminous, S stars might substantially contribute. We explicitly include S0-2 star into the calculations as one of the most luminous and the closest to Sgr A* S stars (Martins et al. 2008; Gillessen et al. 2009a). Dimmer S stars contribute relatively little to the incident ionizing flux, when G2 is far from the pericenter. Their initial mass function (IMF) has the slope $\Gamma = -2.15 \pm 0.3$ (Do et al. 2013). However, the dependence of their bolometric luminosity on mass is very steep $L_\star \propto M_\star^{3.5}$ at $M_\star \lesssim 10 M_\odot$ (e.g. Salaris & Cassisi 2005) and the dependence of the luminosity above the hydrogen ionization threshold is even steeper. Heavy stars with the masses $M_\star > 10 M_\odot$ and the top-heavy IMF (Bartko et al. 2010) are included into the calculation individually.

The incident fluxes at the locations of G2 and Sgr A* are presented in Table 1. The positions of G2 in the picture plane are taken from Phifer et al. (2013), while the inclination angle $i = 118°$ and the longitude of periastron $\omega = 97°$ are taken from Gillessen et al. (2013b). The S0-2 star was far from its pericenter in the years of observations. The incident flux changed by only 30% between 2004 and 2011 despite the G2 cloud moved substantially. The total flux $F_{\rm tot} = 5.2 \times 10^4 {\rm erg\ s^{-1} cm^{-2}}$ and the photon energy density $U_{\rm ph} = 1.7 \times 10^{-6} {\rm erg\ cm^{-3}}$ at Sgr A* in 2011 are an order of magnitude larger than the estimates in Krabbe et al. (1991); Quataert & Loeb (2005), but are much smaller than the flux and the energy density at Sgr A*, when S0-2 passes through its pericenter (Nayakshin 2005).

3.2. *Radiation from the Cloud*

The radiative transfer through the mixture of the ionized gas and the dust is performed with the version 13 of CLOUDY code (Ferland et al. 2013). We effectively consider the stretched cloud to be rectangular and irradiated perpendicular to its longer side from one direction. We compute models with the graphite dust with 10 nm grains and with the ISM dust, which includes a range of grain sizes (Mathis et al. 1977). The former choice is motivated by the high inferred dust temperature, which can only be achieved by the very small grains (Draine 2011; Gillessen et al. 2012). We consider the spherical, tidally distorted, and magnetically arrested cloud shapes. We vary the dust abundance A relative to the ISM (Bohlin et al. 1978) and the cloud radius $R_{\rm init}$ fitting the 2011 IR data for each of the initial cloud densities $n_{\rm init}$. We fit the Brγ luminosity, the ratio $L({\rm HeI})/L({\rm Br}\gamma)$, and the luminosities in M and L' bands. We do not fit the ratio of the Paα luminosity to

TABLE 1
DISTANCES AND INCIDENT FLUXES AT THE LOCATIONS OF G2 AND SGR A* IN DIFFERENT YEARS

Quantity	In 2004 at G2	In 2008 at G2	In 2011 at G2	At G2 pericenter	In 2011 at Sgr A*
Distance from G2 to Sgr A*, arcsec [a]	0.59	0.43	0.30	0.020	⋯
Total flux[b,c], 10^4erg s^{-1}cm^{-2}	3.0 (75%)	3.5 (87%)	4.0 (100%)	5.7 (142%)	5.2 (129%)
S0-2 flux[b], 10^4erg s^{-1}cm^{-2}	0.26 (31%)	0.47 (57%)	0.84 (100%)	2.6 (306%)	2.0 (241%)
Total of IRS16NW, IRS16C, and IRS16SW fluxes[b], 10^4erg s^{-1}cm^{-2}	2.8 (86%)	3.1 (95%)	3.2 (100%)	3.2 (100%)	3.2 (100%)
S0-2 contribution to flux	8.4%	13%	21%	44%	39%

[a]For the orbital inclination angle $i = 118°$ and the longitude of periastron $\omega = 97°$.
[b]Fluxes relative to 2011 are shown in parentheses.
[c]Computed as the sum of the S0-2 flux and 4/3 of the total flux from IRS16NW, IRS16C, and IRS16SW.

the Brγ luminosity, as it is practically constant

$$L(\mathrm{Pa}\alpha)/L(\mathrm{Br}\gamma) = 11.7 - 11.8 \qquad (19)$$

for all computed models. The values $11.7 - 11.8$ are within 2σ from the observed ratio. We consider the transmitted continuum, but check that the reflected continuum is consistent with it to within 10% in each IR band of interest for all computed models. The HeI line shows the largest optical depth τ among the lines of interest, but it is still optically thin with $\tau = 0.03 - 0.1$.

The properties of the spherical models, which provide the best fit to the data at each density, are shown in Figure 1 for the ISM dust (solid lines) and the 10 nm graphite dust (dashed lines). The models with the graphite dust fit the data very well for a wide range of densities $n_{\mathrm{init}} = 3 \times 10^4 - 10^7\mathrm{cm}^{-3}$. The exception is a narrow region of a poor fit around $n_{\mathrm{init}} = 1.5 \times 10^5\mathrm{cm}^{-3}$, where the simulated ratio $L(\mathrm{He}I)/L(\mathrm{Br}\gamma)$ is too high. In turn, the models with the ISM dust favor the low densities around $n_{\mathrm{init}} = 7 \times 10^4\mathrm{cm}^{-3}$, for which the dust content is a fraction $A = 0.7$ of the dust content in the ISM. The high-density models with the ISM dust do not fit the data well as the dust emission becomes too red and the ratio $L(\mathrm{He}I)/L(\mathrm{Br}\gamma)$ becomes too high both owing to a substantial attenuation of the incident radiation by the cloud. The best-fitting cloud mass is around $m_{\mathrm{cloud}} = 10M_{\mathrm{Earth}}$. The observed Ks magnitude $m_{Ks} = 19.7$ is consistent with the non-detection. However, the best-fitting radius $R_{\mathrm{init}} = 5 \times 10^{15}\mathrm{cm} = 40$ mas is larger than the observed spatial extent of the cloud (Gillessen et al. 2012). No models with the ISM dust are consistent with the observed radius and only the high-density models with the 10 nm graphite grains are marginally consistent.

The properties of the magnetically arrested models (blue/dark lines) and the tidally distorted models (green/light lines), which provide the best fit to the data at each density, are shown in Figure 2 for the ISM dust. The best-fitting initial densities for these shapes are $n_{\mathrm{init}} = 3.5 \times 10^4\mathrm{cm}^{-3}$ and $n_{\mathrm{init}} = 1.5 \times 10^4\mathrm{cm}^{-3}$, respectively. These densities correspond to the same cloud density $n = (6-8) \times 10^4\mathrm{cm}^{-3}$ in 2011. The best-fitting masses of the cloud m_{cloud}, the relative dust abundances A, and the simulated apparent Ks magnitudes practically coincide with the values for the best-fitting spherical model. The initial cloud radii $R_{\mathrm{init}} \lesssim 6 \times 10^{15}$ cm are consistent with the observations due to the shrinking of the cloud in the perpendicular direction. We discuss the consistency with the size observations in more detail below for the best-fitting model.

The critical test for any cloud model is the ability to reproduce the IR observations made in different years. In Figure 3 we present the simulated normalized Brγ luminosity, the ratio $L(\mathrm{He}I)/L(\mathrm{Br}\gamma)$, and the absolute magnitude $M_{L'}$ for the spherical clouds in the years 2004, 2008, and 2011. The mod-

els tested are the ones, which provide the best fits to the 2011 data for each initial density. We find two large classes of the outcomes different by the optical depth to the irradiating ionizing continuum. The optically thin models with low n_{init} do not substantially attenuate the ionizing flux and maintain the high gas temperature $T_{\mathrm{cloud}} = (0.7 - 1.2) \times 10^4$ K throughout the cloud. The optically thick models with high n_{init} absorb most of the ionizing radiation, so that their temperature drops to $T_{\mathrm{cloud}} \lesssim 5 \times 10^3$ K on the far side of the cloud. The latter models emit most of their IR flux near the irradiated side of the cloud. The optically thin spherical clouds exhibit practically constant with time $L(\mathrm{Br}\gamma)$. Since the cooling function depends strongly on the temperature $\Lambda(T) \propto T^\delta$ with $\delta \sim 5$ at $T \sim 10^4$ K, then the increase by 30% of the irradiating flux between the years 2004 and 2011 leads to only a 6% temperature rise. The line emissivity (Draine 2011)

$$\alpha(\mathrm{Br}\gamma) \propto T^{-1}n^2 \qquad (20)$$

then decreases by 6%, which explains the trend at the lowest simulated densities. The increase of $L(\mathrm{Br}\gamma)$ in the optically thick group simply follows the rise of the irradiating flux, since both the density and the cross-section of the spherical cloud remain constant. The ratio $L(\mathrm{He}I)/L(\mathrm{Br}\gamma)$ slightly decreases in the optically thin models between 2008 and 2011 consistently with the observations. The flux emitted by the dust always positively correlates with the incident flux and the source becomes brighter with time in L' band. The temporal dependence of the M-band absolute magnitude directly follows the dependence of the L' magnitude shown in the bottom panel. The best-fitting model lies within the optically thin group and thus not only explains the spectrum in 2011, but also reproduces the observations in the earlier years. The models with the ISM dust and the graphite dust behave similarly.

In Figure 4 we present the temporal behavior of the tidally distorted and the magnetically arrested models with the ISM dust. The models tested are the ones, which provide the best fits to the 2011 data for each initial density. The tidally distorted shapes show distinct behaviors for the optically thin and the optically thick groups. The Brγ luminosity rises steeply in the optically thin group, which includes the best-fitting model. This is due to a large density increase with time and is inconsistent with the observations. The ratio $L(\mathrm{He}I)/L(\mathrm{Br}\gamma)$ increases with time in a tidally distorted model. In turn, the optically thin and the optically thick magnetically arrested models behave similarly, owing to the less dramatic temporal changes of density. The rise of the Brγ luminosity by 1.3 from 2004 to 2011 is marginally consistent with the observations of this line (Gillessen et al. 2013b). We conduct the linear regression over the observed values of $L(\mathrm{Br}\gamma)$ and find that the variations by 30% between 2004 and 2011 are near the boundary
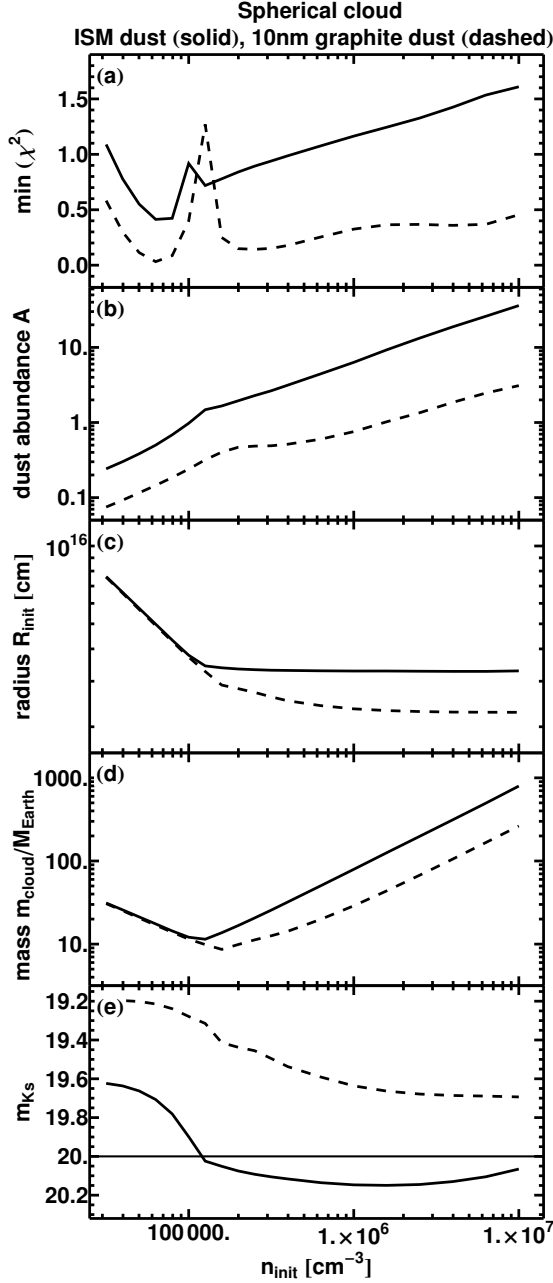
Spherical cloud
ISM dust (solid), 10nm graphite dust (dashed)

Magnetically arrested cloud (blue/dark)
Tidally distorted cloud (green/light)

FIG. 1.— Properties of the best-fitting spherical clouds for the different densities $n_{\rm init}$: the minimum χ^2 for fitting $L({\rm Br}\gamma)$, $L({\rm He}I)/L({\rm Br}\gamma)$, $M_{L'}$, and M_M (panel a), the relative amount of dust A (panel b), the initial cloud radius $R_{\rm init}$ (panel c), the cloud mass measured in the masses of the Earth $m_{\rm cloud}/M_{\rm Earth}$ (panel d), and the simulated apparent Ks magnitude m_{Ks} (panel e). Shown are the models with the ISM dust (solid) and the 10 nm graphite dust (dashed).
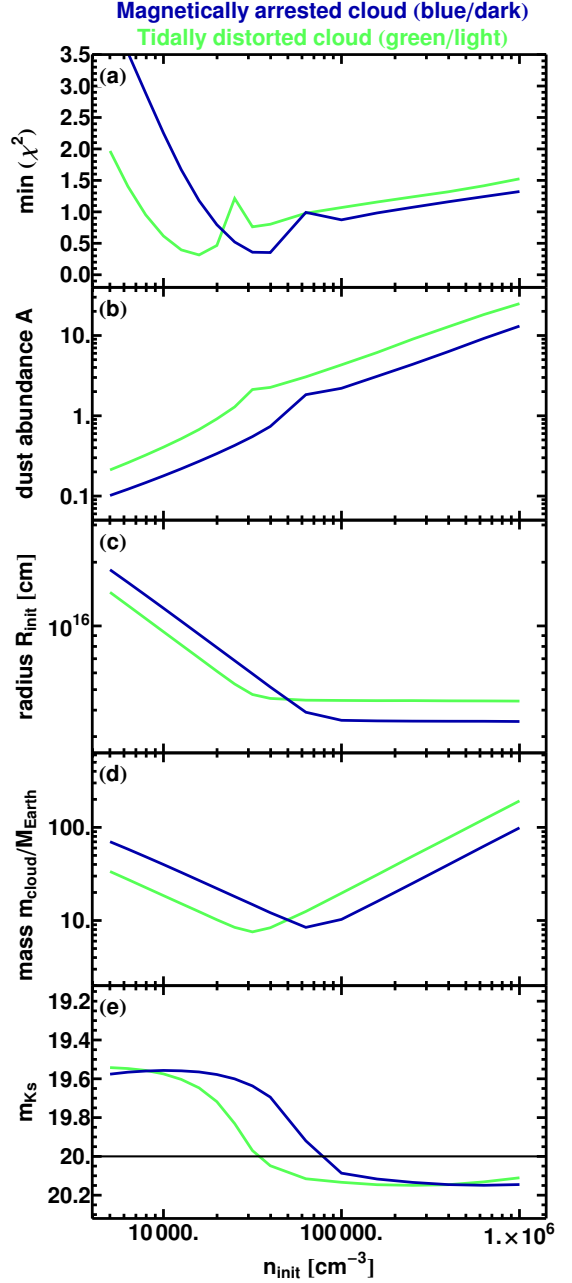
FIG. 2.— Properties of the best-fitting magnetically arrested (blue/dark lines) and tidally distorted (green/light lines) cloud models with the ISM dust for the different initial densities $n_{\rm init}$: the minimum χ^2 for fitting $L({\rm Br}\gamma)$, $L({\rm He}I)/L({\rm Br}\gamma)$, $M_{L'}$, and M_M (panel a), the relative amount of dust A (panel b), the initial cloud radius $R_{\rm init}$ (panel c), the cloud mass measured in the masses of the Earth $m_{\rm cloud}/M_{\rm Earth}$ (panel d), and the simulated apparent Ks magnitude m_{Ks} (panel e).

of the 90% confidence interval. The optically thin magnetically arrested models have a small negative temporal slope of the $L({\rm He}I)/L({\rm Br}\gamma)$ ratio in agreement to observations.

3.3. *Best-fitting Magnetically Arrested Model*

The best-fitting magnetically arrested cloud model has the density, the radius, and the relative dust abundance

$$n_{\rm init} = 3.6 \times 10^4 {\rm cm}^{-3}, \ R_{\rm init} = 5.5 \times 10^{15} {\rm cm} = 43 {\rm mas}, \ A = 0.65,$$
$$(21)$$

respectively, and reaches $\chi^2 = 0.33$. This relative dust abundance corresponds to the dust-to-gas ratio 4.14×10^{-3} by mass, while the total mass of such cloud is $m_{\rm cloud} = 13 M_{\rm Earth}$. The cloud with the initial size $R_{\rm init} = 43 {\rm mas}$ shrinks in the perpendicular direction to $\rho = 25$ mas and $\rho = 20$ mas in 2008 and 2011, respectively, which is consistent with the direct size measurements (Gillessen et al. 2012). However, the radial stretching to the half-length $L = 78$ mas produces the projected size $R = 37$ mas in the picture plane in 2011 for the inclination angle $i = 118°$ and the longitude of periastron $\omega = 97°$. The
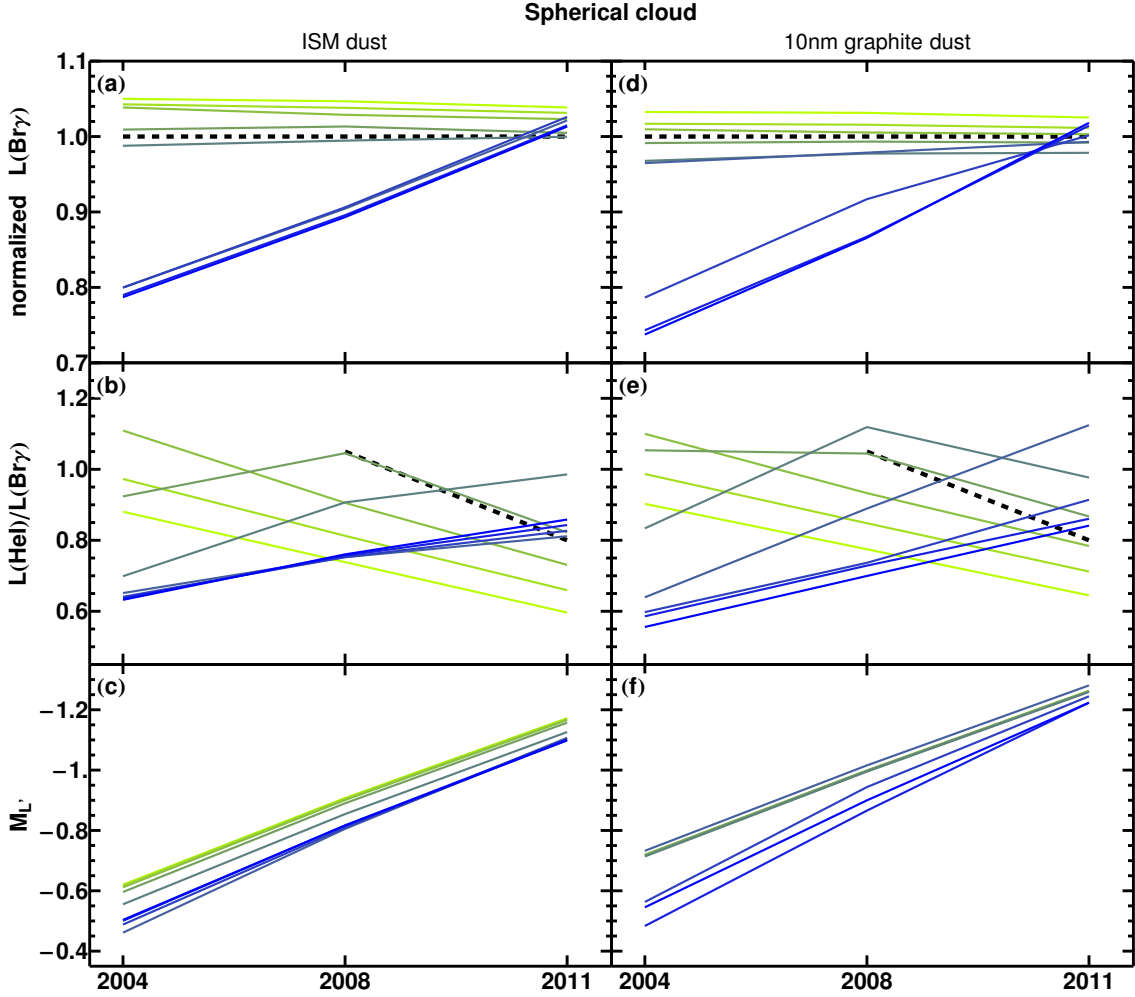
Spherical cloud

FIG. 3.— Temporal dependence of quantities in the best-fitting spherical models for a range of the initial cloud densities $n_{\rm init}$: the Brγ luminosity normalized to the observed line luminosity (top row), the ratio $L({\rm HeI})/L({\rm Br}\gamma)$ (middle row), and the absolute magnitude $M_{L'}$ (bottom row). The models with the initial densities $\log(n_{\rm init}, {\rm cm}^{-3}) = 4.6, 4.7, 4.8, 4.9, 5.$ correspond to the optically thin group (light/yellow lines), while the models with the initial densities $\log(n_{\rm init}, {\rm cm}^{-3}) = 5.1, 5.2, 5.3, 5.4$ correspond to the optically thick group (dark/blue lines). The left column shows the results for the ISM dust and the right column shows the results for the 10 nm graphite dust.

velocity spread between two ends of the cloud is

$$\Delta v \approx \sqrt{\frac{2GM_{\rm BH}}{r^3}} L \sin i \sin \omega, \qquad (22)$$

when the object is on a highly eccentric orbit far from the pericenter. The values $\Delta v = 333 {\rm km \, s}^{-1}$ in 2011 and $\Delta v = 205 {\rm km \, s}^{-1}$ in 2008 for the chosen orbital parameters perfectly agree with the intrinsic integrated full-width at half-maximum velocity $\Delta v_{\rm obs} = 350 \pm 40 {\rm km \, s}^{-1}$ in 2011 and $\Delta v_{\rm obs} = 210 \pm 24 {\rm km \, s}^{-1}$ in 2008 reported in Gillessen et al. (2012) for the head of the cloud. The consistency of the radial velocity and the seeming inconsistency of the apparent cloud size can be ascribed to either the uncertainty of the size measurement emphasized in Gillessen et al. (2013b) or the uncertainty of the G2 orbital parameters or the modeling approximations in this work. The spectrum of this model in 2011 is shown in Figure 5 (blue line). The modified blackbody spectrum (red line) represents the contribution of the smallest dust grains with sizes $6-13$ nm, which have the temperature $T_{\rm dust} = 489$ K. The larger grains, which have the lower temperatures $T_{\rm dust} = 300 - 450$ K, contribute substantially to the

observed emission in the M and L' bands. The emissivity of the smallest particles ϵ_ν is given by the modified blackbody spectrum (Draine 2011)

$$\epsilon_\nu \propto \nu^2 B_\nu \propto \nu^5 \left(\exp \left[\frac{h\nu}{k_B T_{\rm dust}} \right] - 1 \right)^{-1}, \qquad (23)$$

where B_ν is the blackbody spectrum.

The cloud is magnetically arrested at a distance $r_{\rm init} = 1$ arcsec, when its magnetization is $\sigma \sim 10$ according to the formula (13). The ambient hot gas density and temperature are approximately (Baganoff et al. 2003; Shcherbakov & Baganoff 2010)

$$n_{\rm gas} = 130 \left(\frac{r}{\rm arcsec} \right)^{-1} {\rm cm}^{-3} \qquad (24)$$

and

$$T_{\rm gas} = 3 \times 10^7 \left(\frac{r}{\rm arcsec} \right)^{-1} {\rm K}. \qquad (25)$$

The gas pressure of the best-fitting magnetically arrested model is about 10% of the ambient gas pressure at the formation $n_{\rm init} T_{\rm cloud} \sim 0.1 n_{\rm gas} T_{\rm gas}$, but the cloud magnetic force
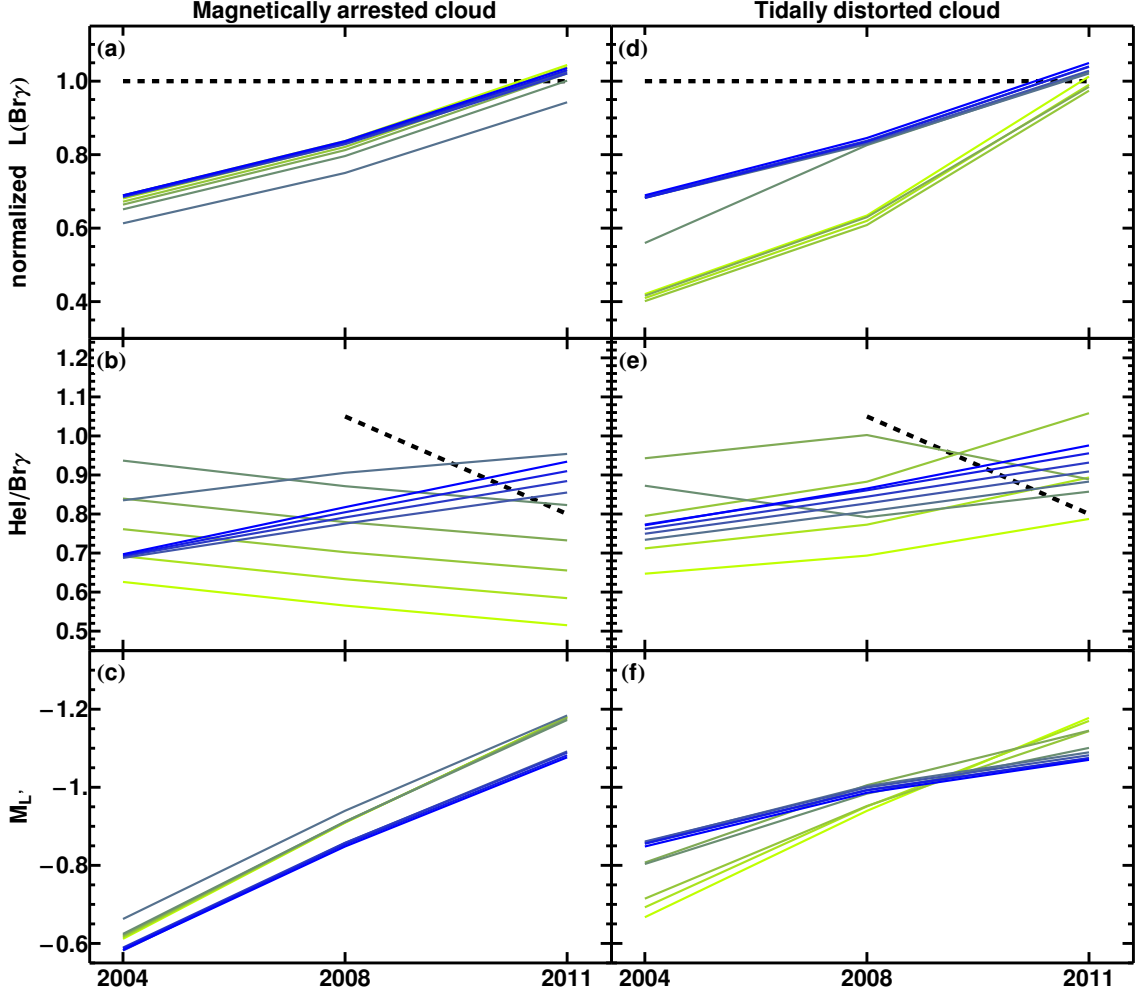
FIG. 4.— Temporal dependence of quantities in the best-fitting magnetically arrested (left column) and tidally distorted (right column) models for a range of the initial cloud densities $n_{\rm init}$: the Brγ luminosity normalized to the observed line luminosity (top row), the ratio $L({\rm He}I)/L({\rm Br}\gamma)$ (middle row), and the absolute magnitude $M_{L'}$ (bottom row). The models with the initial densities $\log(n_{\rm init}, {\rm cm}^{-3}) = 4.2, 4.3, 4.4, 4.5, 4.6$ correspond to the optically thin group (light/yellow lines), while the models with the initial densities $\log(n_{\rm init}, {\rm cm}^{-3}) = 4.8, 5., 5.2, 5.4, 5.6$ correspond to the optically thick group (dark/blue lines).
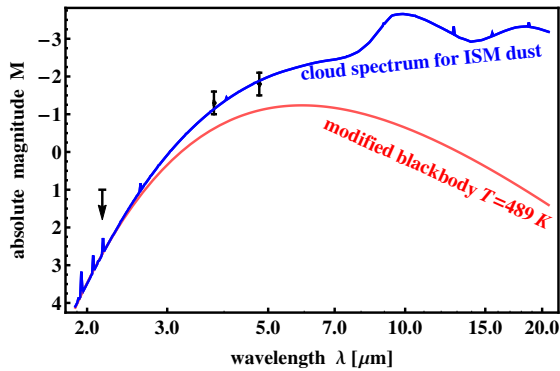

FIG. 5.— IR spectrum of the best-fitting magnetically arrested model in 2011 (blue/dark line), modified blackbody contribution of the smallest dust grains (red/light line), and observations reported in Gillessen et al. (2012) (error bars and upper limit in black/dark).

$F_{\rm magn}$ is comparable to the ambient gas force $F_{\rm out}$. However, the magnetic force grows faster inwards, which justifies neglecting the ambient gas in calculation of the shape. Let us estimate the radiation from such cloud, when it passes through the pericenter.

4. RADIATION DURING PERICENTER PASSAGE

4.1. *Bow Shock Radio, IR, and X-ray Emission*

As the cloud passes through the pericenter, it creates a bow shock with a Mach number $\mathcal{M} \approx 2$, which accelerates the electrons (Narayan et al. 2012; Sądowski et al. 2013). The accelerated electrons radiate synchrotron emission, most notably in the radio band. The particle distribution was formerly estimated to be

$$\frac{dN}{d\gamma} \approx 2 \times 10^{49} \gamma^{-2.2}, \quad \gamma \geq 2 \qquad (26)$$

for the fiducial efficiency 5% and the cloud perpendicular radius $\rho_{\rm Ram} = 10^{15}$ cm at the pericenter. The ambient hot gas density is $n \approx 4 \times 10^3 {\rm cm}^{-3}$, the temperature is $T \approx 10^9$ K, and the ambient magnetic field is $B \approx 0.05$ G at the adopted pericenter radius $r_p = 2000 r_{\rm S}$. The corresponding perpendicular radius of the best-fitting magnetically arrested cloud is $\rho_p = 5.0 \times 10^{14} {\rm cm} = 400 r_{\rm S}$ according to equation (11). Then we estimate the normalization constant of the particle distribution to be a factor of $(\rho_{\rm Ram}/\rho_p)^2 = 4$ lower. The particle distribution with the slope $p = 2.2$ does not continue till the infinite Lorentz factor, but breaks at a characteristic $\gamma_{\rm cool}$ de-

termined by cooling (Yuan et al. 2003). The synchrotron cooling timescale is

$$t_{\text{synch}} = \frac{6\pi m_e c}{\sigma_T \gamma B^2}, \tag{27}$$

while the characteristic dynamical timescale is

$$t_{\text{dyn}} \sim 2 t_{\text{ff}} = 4 \text{months}, \tag{28}$$

so that the cooling break is at

$$\gamma_{\text{cool}} \sim 3 \times 10^4. \tag{29}$$

The modified electron distribution is

$$\frac{dN}{d\gamma} \approx 5 \times 10^{48} \begin{cases} \gamma^{-2.2}, & \text{for } \gamma \leq \gamma_{\text{cool}} \\ \gamma_{\text{cool}} \gamma^{-3.2}, & \text{for } \gamma > \gamma_{\text{cool}}. \end{cases} \tag{30}$$

The peak frequency of the synchrotron emission is

$$\nu = \frac{3}{4\pi} \gamma^2 \frac{eB}{m_e c}, \tag{31}$$

which corresponds to the frequency $\nu_{\text{cool}} = 2.7 \times 10^{14}$ Hz and the near-IR wavelength $\lambda_{\text{cool}} = 1.1\mu$m for the electrons at the cooling break. Averaging the synchrotron emissivity (Rybicki & Lightman 1979) over the pitch angles we obtain the specific luminosity

$$L_\nu = 5 \times 10^{48} \frac{\sqrt{3\pi}e^3 B}{2m_e c(p+1)} \left(\frac{2\pi m_e c\nu}{3eB} \right)^{-p/2+1/2} g, \tag{32}$$

where the constant equals $g = \Gamma(p/4 + 5/4)\Gamma(p/4 + 19/12)\Gamma(p/4 - 1/12)/\Gamma(p/4 + 7/4)$ with a gamma-function $\Gamma(x)$. The optically thin specific flux is $F_\nu = L_\nu/(4\pi d^2)$, which gives

$$F_\nu \approx 2.7 \left(\frac{\nu}{\text{GHz}} \right)^{-0.6} \text{Jy for } \lambda \geq 1.1\mu\text{m} \tag{33}$$

below the cooling break. This estimate is several times lower than the prediction in Narayan et al. (2012).

The specific flux at $\nu = 22$ GHz is expected to increase by only $\Delta F_\nu = 0.4$ Jy, which is lower than the quiescent level of Sgr A* at that frequency (Shcherbakov et al. 2012). The G2 radio flux is comparable to the Sgr A* flux at the lower frequencies $\nu \lesssim 14$ GHz, but the observational error at these ν is also high (Bower et al. 2013). The bow-shock K-band flux is

$$F_\nu(2\mu\text{m}) \approx 2\text{mJy}, \tag{34}$$

which is also below the quiescent level of Sgr A* (Dodds-Eden et al. 2011) and is difficult to measure. The maximum electron Lorentz factor

$$\gamma_{\text{max}} = \left(\frac{6\pi e}{\sigma_T B} \right)^{1/2} \gtrsim 10^8 \tag{35}$$

is determined by the equality of the cooling time and the acceleration time (Pe'er & Waxman 2005). Such high Lorentz factors are found in the supernova shock remnants, which appear to produce X-ray synchrotron emission (Reynolds 1996). The electrons with relatively moderate Lorentz factors $\gamma \sim 10^6$ produce the X-rays at the G2 pericenter. The specific synchrotron flux above the cooling break behaves as $F_\nu \propto \nu^{-1.1}$ and the estimated intrinsic luminosity is

$$\nu L_\nu = 1.5 \times 10^{34} \left(\frac{\nu}{4\text{keV}} \right)^{-0.1} \text{erg s}^{-1} \text{ for } \lambda < 1.1\mu\text{m}. \tag{36}$$

The predicted power $\nu L_\nu = 1.5 \times 10^{34}$ at $\nu = 4$ keV is several times above the quiescent unabsorbed luminosity of Sgr A* $L_X \sim 3 \times 10^{33}$erg s^{-1} (Baganoff et al. 2003; Wang et al. 2013), but much below the luminosity $L_X = 4 \times 10^{35}$erg s^{-1} of the magnetar, which turned on near Sgr A* on 2013 April 23 (Kennea et al. 2013; Rea et al. 2013).

The bow shock should have passed through the pericenter around 2013 March according to Sądowski et al. (2013) ahead of the CM. The specific flux increase by $\Delta F_\nu = 0.4$ Jy at 22 GHz was indeed observed in 2013 April (Tsuboi et al. 2013), but the observations in 2013 June by Bower et al. (2013) showed that Sgr A* returned to the mean level of radio flux. As the intrinsic variability of Sgr A* is about 0.4 Jy at 22 GHz (Shcherbakov et al. 2012), then the rise observed in 2013 April may have been unrelated to the cloud, especially since no substantial flux increase was detected at the lower frequencies $\nu = 1.5 - 14$ GHz (Bower et al. 2013). No substantial X-ray flux increase was reported either from the Sgr A* region before the magnetar turned on in 2013 April (Rea et al. 2013).

However, we predict an even earlier bow shock pericenter passage. All computed magnetically arrested and tidally distorted models have a much larger cloud half-length $L \approx 0.3$ arcsec at the pericenter compared to the estimate in Sądowski et al. (2013). Then the time between the bow shock passes through the pericenter and the CM passes is

$$\Delta t = 1.8 \text{years}. \tag{37}$$

The flux increase could have happened in 2012 and lasted for about the dynamical time $t_{\text{dyn}} \sim 4$ mo at the frequencies above the cooling break. An increase of the quiescent Sgr A* X-ray luminosity by up to 10^{33}erg s^{-1} is measurable in the 2012 data from *Chandra* X-ray visionary project (PIs: Baganoff, Nowak, and Markoff) (Nowak et al. 2012). The detailed analysis of these data can place a useful limit on the particle acceleration to the high Lorentz factors by the G2 cloud bow shock.

The ratio of the ambient magnetic field energy density to the radiation energy density is about 10^{-2} at the pericenter. Then the inverse Compton power is 100 times lower than the synchrotron power for the same γ, thus the particles cool via the synchrotron radiation. The inverse Compton emission power (Rybicki & Lightman 1979)

$$L_C = \frac{4}{3}\sigma_T c\gamma^2 U_{\text{ph}} \tag{38}$$

peaks at a frequency

$$\nu_C = \gamma^2 \nu_{\text{ph}}, \tag{39}$$

where ν_{ph} is a frequency of the seed optical and ultraviolet photons. The inverse Compton X-rays are produced by the electrons with the Lorentz factors $\gamma = 20 - 60$. Convolution of the electron distribution with the photon field gives the inverse Compton X-ray luminosity

$$L_{X,C}(2 - 10\text{keV}) = 3 \times 10^{30}\text{erg s}^{-1} \tag{40}$$

much below the quiescent level of Sgr A*. The inverse Compton scattering of the dust IR emission produces an even lower X-ray power, since the particle acceleration site is offset from the CM.

4.2. *Emission from the Bulk of the Cloud*

When the tidally disrupted object is not magnetized, then the tidal shock occurs at a specific location, where the orbital planes of the independently moving cloud particles intersect (Carter & Luminet 1983; Luminet & Marck 1985). The shock can locally heat the gas up to the relatively high temperature, despite the compressed gas cools efficiently on the way to the pericenter (Saitoh et al. 2012). However, the tidal shock does not occur in the magnetically arrested model, where the cloud is supported by the magnetic pressure. Instead, relatively gradual heating takes place over the entire volume of the cloud.

The best-fitting magnetically arrested model has the density $n_{peri} = 7 \times 10^4 cm^{-3}$, the magnetic field $B_{peri} \approx 0.7$ G, and the Alfven crossing time $t_A \approx 1$ mo at the pericenter. The self-consistency of the model requires that the magnetic field dissipation time is much longer than the Alfven time $t_{diss} \gtrsim 10 t_A = 0.8$ yr. Then the volume heating rate is

$$Q_{vol} \lesssim \frac{B_{peri}^2}{8\pi} t_{diss}^{-1} \sim 8 \times 10^{-10} erg\ s^{-1} cm^{-3}. \quad (41)$$

Heating is substantial only over a part of the cloud near the pericenter with the length $\Delta L \sim 2R_p$, since Q_{vol} depends steeply on the distance to Sgr A*.

Gillessen et al. (2012, 2013b) expect the interaction with the hot ambient medium to drive a strong shock into the cloud, since the gas pressure of the cloud is much less than the ambient pressure. However, the ratio of the ambient gas pressure to the cloud magnetic pressure is

$$\frac{p_{gas}}{p_{magn}} = \frac{8\pi n_{gas} k_B T_{gas}}{B_{peri}^2} \approx 0.07 \quad (42)$$

at the pericenter in the magnetically arrested model. The ratio is much less than unity and the cloud is magnetically supported against the ambient hot gas. Then we do not expect the shock or the corresponding X-ray radiation. The equation (42) also justifies neglecting the ambient gas force F_{out} in the force balance given by the equation (10).

We simulate the emission from the part of the cloud near the pericenter heated by the magnetic field dissipation. The model with the dissipation time $t_{diss} = 10 t_A$ produces the hot gas at $T \approx 0.7$ keV, which emits practically no hydrogen or helium lines. The resultant X-ray luminosity is $L_X (2-10 keV) = 5 \times 10^{32} erg\ s^{-1}$, much below the quiescent level of Sgr A*. The dust temperature reaches $T_{dust} = (1-1.5) \times 10^3$ K, which is barely below the sublimation threshold (Guhathakurta & Draine 1989; Ferland et al. 2013). Such dust manifests as an IR source with the apparent magnitudes $m_M = 13$, $m_{L'} = 13$, and $m_{K_s} = 14.6$, which are about 2 mag brighter in M and L' band and up to 5 mag brighter than the upper limit in K_s band, when compared to 2011 data. The model with a longer dissipation time $t_{diss} = 20 t_A$ has a slightly lower temperature $T \approx 0.45$ keV, but a much lower X-ray luminosity $L_X (2-10 keV) = 1 \times 10^{32}$ erg. The corresponding apparent magnitudes are $m_M = 13.6$, $m_{L'} = 13.6$, and $m_{K_s} = 15.6$. The gas cools more efficiently for the larger dissipation times $t_{diss} \gtrsim 20 t_A$, so that the gas temperature settles to $T = (2-6) \times 10^4$ K. This drives Brγ luminosity down from the case of no extra heating. If only the ionizing radiation heats the gas, then the simulated Brγ luminosity is $L(Br\gamma) \sim 2 \times 10^{31} erg\ s^{-1}$ at the pericenter due to the larger cloud density and the higher S0-2 flux, which is 2 times higher than the observed level. Even small heating with $t_{diss} \gtrsim 20 t_A$ decreases the Brγ emissivity in the optically

thin models, which could lead to a constant or a decreasing Brγ flux from the cloud as it passes through the pericenter.

5. DISCUSSION AND CONCLUSIONS

In the present paper we report the line and the dust diagnostics of the G2 object, hypothesized to be a cloud, moving towards Sgr A* in the Galactic Center. We consider three cloud shapes: the spherical, tidally distorted, and magnetically arrested. The spherical shape can be preserved by the cloud in the presence of the central star. The tidally distorted shape is appropriate for the unmagnetized cloud. The magnetically arrested regime is representative of the magnetized cloud behavior. We identify the optically thin and the optically thick groups of models based on the optical depth to the incident ionizing radiation. The models perform differently, when compared to the data. The optically thin spherical models show the constant Brγ luminosity, despite Scoville & Burkert (2013) expects only the collisionally ionized gas with the internal energy source to reproduce $L(Br\gamma) = const$. However, the spherical models overestimate the cloud size above the observed value. The optically thin tidally distorted shapes show a relatively large increase of $L(Br\gamma)$ inconsistent with the observations, while the optically thick tidally distorted shapes provide worse spectral fits. All computed magnetically arrested models show the relatively weak increase of $L(Br\gamma)$ with time marginally consistent with the observations.

The best-fitting magnetically arrested model has the initial density $n_{init} = 3.6 \times 10^4 cm^{-3}$, the initial radius $R_{init} = 5.5 \times 10^{15} cm = 43$mas, the cloud mass $m_{cloud} = 13 M_{Earth}$, and the relative dust abundance $A = 0.65$. Such cloud forms as a spherical object at the distance $r_{init} = 1$ arcsec from Sgr A*. From the place of formation to the pericenter the cloud is in the perpendicular balance of the magnetic force and the gravitational force. This model reaches an excellent agreement with the Brγ luminosity, the ratio $L(HeI)/L(Br\gamma)$, and the L' and M magnitudes observed in 2011. It is marginally consistent with the luminosities and the magnitudes reported in 2004 and 2008. The perpendicular cloud size agrees with the observed size in 2008 and 2011, while the radial stretching of the cloud leads to the projected size somewhat larger than the observed. However, the correspondent spread of the radial velocity matches the observations in 2008 and 2011. The agreement of the velocity spread and the seeming overprediction of the cloud size may find explanation in the uncertainties of the observations or in the approximations of modeling.

The L' band emission is simulated to grow by $\Delta M_{L'} = 0.5$ mag from 2004 till 2011 and is expected to reach $m_{L'} = 14.3$ mag at the pericenter as the incident flux further increases by 40% compared to 2011 (see Table 1). The dim S stars provide an additional contribution to the incident flux at the pericenter due to the rising inwards surface brightness profile $\Sigma \propto r^{-0.93\pm0.09}$ (Do et al. 2013). They are not expected to produce a substantial number of the ionizing photons, but their radiation is reprocessed by the dust. However, the internal dust heating may dominate the heating by the incident flux. The dissipation of the magnetic energy near the pericenter raises the temperature of the gas, which collisionally heats the dust. As a result, the dust emits substantially more IR light and the cloud could reach observed magnitude up to $m_{L'} = 13$. The observations of the pericenter passage in the IR band probe the magnetic energy dissipation rate, though such observations are difficult due to the source confusion near Sgr A* (Phifer et al. 2013).

The bow shock region is expected to produce a distinct ra-

diative signature. The bow shock should brighten in the radio band and the X-rays about $\Delta t \sim 1.8$ yrs before the CM passes through the pericenter. The brightening lasts for the dynamical time $t_{\text{dyn}} \sim 4$ mo at the wavelengths $\lambda < 1.1\mu$m affected by the synchrotron cooling. The best-fitting magnetically arrested model predicts the specific flux of $F_\nu = 0.4$ Jy at $\nu = 22$ GHz and the X-ray luminosity $\nu L_\nu = 1.5 \times 10^{34}$erg s^{-1} at $\nu = 4$ keV. This radio flux is a factor of several lower than the prediction in Narayan et al. (2012) owing mainly to the smaller cross-section. However, the predicted emission is still uncertain by a factor of several, since the particle acceleration efficiency is not known (Narayan et al. 2012). The positive detection or the non-detection of the radio flux from G2 constrain the product of the particle acceleration efficiency by the bow shock cross-section. The X-ray observations constrain the acceleration of particles to the large Lorentz factors $\gamma \sim 10^6$. Our suggestion of the very early bow shock pericenter passage is strengthened by the achieved match to the observed spread of the cloud radial velocity.

Following the pericenter passage the cloud is disrupted by the combined effects of the Kelvin-Helmholtz and Rayleigh-Taylor instabilities, the external pressure, the differential gravitational force, and the conductive heating of the cloud (Gillessen et al. 2012; Burkert et al. 2012; Anninos et al. 2012; Saitoh et al. 2012; Ballone et al. 2013). We predict a factor of 4 larger mass of the cloud compared to the estimate in Gillessen et al. (2012). The resultant BH accretion rate and the accretion flow luminosity are also higher (Mościbrodzka et al. 2012), if the disruption dynamics is unchanged. The heavier clouds are to be tested with the future numerical simulations of G2.

Despite the agreement with the data, the best-fitting magnetically arrested model might not fully represent the G2 cloud. We considered three idealized cases for the shape, while more options are possible. If the magnetization is relatively low $\sigma < 10$, then the cloud starts off as the tidally distorted shape, while closer to the pericenter it switches to the magnetically arrested regime. However, if the switching happens after 2004, then such hybrid models may exhibit a large rise of the Brγ luminosity inconsistent with the observations. The magnetized cloud may not be closely follow the computed magnetically arrested shape. If the magnetic field in the cloud dissipates on the dynamical timescale, then the object approaches the denser tidally distorted shape. Such models are similarly disfavored by the observations. Finally, the dynamical effects acting on the cloud may reduce its mass. Then $L(\text{Br}\gamma)$ could rise less steeply or even be constant with time in the magnetically arrested models, so that the better consistency with the observations is reached.

6. ACKNOWLEDGEMENTS

REFERENCES

Anninos, P., Fragile, P. C., Wilson, J., & Murray, S. D. 2012, ApJ, 759, 132
Baganoff, F. K., et al. 2003, ApJ, 591, 891
Ballone, A., et al. 2013, e-print arXiv:1305.7238
Bartko, H., et al. 2010, ApJ, 708, 834
Biskamp, D. 2003, Magnetohydrodynamic Turbulence (Cambridge, UK: Cambridge University Press)
Bohlin, R. C., Savage, B. D., & Drake, J. F. 1978, ApJ, 224, 132
Bower, G. C., Brunthaler, A., & Falcke, H. 2013, The Astronomer's Telegram, 5159, 1
Burkert, A., Schartmann, M., Alig, C., Gillessen, S., Genzel, R., Fritz, T. K., & Eisenhauer, F. 2012, ApJ, 750, 58
Carter, B., & Luminet, J.-P. 1983, A&A, 121, 97
Clavel, M., Terrier, R., Goldwurm, A., Morris, M. R., Ponti, G., Soldi, S., & Trap, G. 2013, eprints arXiv:1307.3954
Cuadra, J., Nayakshin, S., & Martins, F. 2008, MNRAS, 383, 458
Cuadra, J., Nayakshin, S., Springel, V., & Di Matteo, T. 2005, MNRAS, 360, L55
Czerny, B., Kunneriath, D., Karas, V., & Das, T. K. 2013, A&A, 555, A97
Do, T., Lu, J. R., Ghez, A. M., Morris, M. R., Yelda, S., Martinez, G. D., Wright, S. A., & Matthews, K. 2013, ApJ, 764, 154
Dodds-Eden, K., et al. 2011, ApJ, 728, 37
Draine, B. T. 2011, Physics of the Interstellar and Intergalactic Medium (Princeton University Press)
Ferland, G. J., Korista, K. T., Verner, D. A., Ferguson, J. W., Kingdon, J. B., & Verner, E. M. 1998, PASP, 110, 761
Ferland, G. J., et al. 2013, Revista Mexicana de Astronomia y Astrofisica, 49, 137
Fritz, T. K., et al. 2011, ApJ, 737, 73
Ghez, A. M., et al. 2008, ApJ, 689, 1044
Gillessen, S., Eisenhauer, F., Fritz, T. K., Bartko, H., Dodds-Eden, K., Pfuhl, O., Ott, T., & Genzel, R. 2009a, ApJ, 707, L114
Gillessen, S., Eisenhauer, F., Trippe, S., Alexander, T., Genzel, R., Martins, F., & Ott, T. 2009b, ApJ, 692, 1075
Gillessen, S., et al. 2012, Nature, 481, 51
—. 2013a, ApJ, 763, 78
—. 2013b, ApJ, 774, 44
Guhathakurta, P., & Draine, B. T. 1989, ApJ, 345, 230

Kennea, J. A., et al. 2013, ApJ, 770, L24
Krabbe, A., Genzel, R., Drapatz, S., & Rotaciuc, V. 1991, ApJ, 382, L19
Lu, J. R., Ghez, A. M., Hornstein, S. D., Morris, M. R., Becklin, E. E., & Matthews, K. 2009, ApJ, 690, 1463
Luminet, J.-P., & Marck, J.-A. 1985, MNRAS, 212, 57
Martins, F., Genzel, R., Hillier, D. J., Eisenhauer, F., Paumard, T., Gillessen, S., Ott, T., & Trippe, S. 2007, A&A, 468, 233
Martins, F., Gillessen, S., Eisenhauer, F., Genzel, R., Ott, T., & Trippe, S. 2008, ApJ, 672, L119
Mathis, J. S., Rumpl, W., & Nordsieck, K. H. 1977, ApJ, 217, 425
Meyer, F., & Meyer-Hofmeister, E. 2012, A&A, 546, L2
Miralda-Escudé, J. 2012, ApJ, 756, 86
Mościbrodzka, M., Shiokawa, H., Gammie, C. F., & Dolence, J. C. 2012, ApJ, 752, L1
Murray-Clay, R. A., & Loeb, A. 2012, Nature Communications, 3
Narayan, R., Özel, F., & Sironi, L. 2012, ApJ, 757, L20
Nayakshin, S. 2005, A&A, 429, L33
Nowak, M. A., et al. 2012, ApJ, 759, 95
Oke, J. B. 1974, ApJS, 27, 21
Paumard, T., et al. 2006, ApJ, 643, 1011
Pe'er, A., & Waxman, E. 2005, ApJ, 628, 857
Phifer, K., et al. 2013, ApJ, 773, L13
Quataert, E., & Loeb, A. 2005, ApJ, 635, L45
Rea, N., et al. 2013, eprints arXiv:1307.6331
Reynolds, S. P. 1996, ApJ, 459, L13
Rybicki, G. B., & Lightman, A. P. 1979, Radiative Processes in Astrophysics (New York: Wiley)
Saitoh, T. R., et al. 2012, eprint arXiv:1212.0349
Salaris, M., & Cassisi, S. 2005, Evolution of Stars and Stellar Populations (Wiley-VCH)
Sądowski, A., Sironi, L., Abarca, D., Guo, X., Özel, F., & Narayan, R. 2013, MNRAS
Scoville, N., & Burkert, A. 2013, ApJ, 768, 108
Shcherbakov, R. V. 2008, ApJS, 177, 493
Shcherbakov, R. V., & Baganoff, F. K. 2010, ApJ, 716, 504
Shcherbakov, R. V., Penna, R. F., & McKinney, J. C. 2012, ApJ, 755, 133
Shvartsman, V. F. 1971, Soviet Ast., 15, 377

Tsuboi, M., et al. 2013, The Astronomer's Telegram, 5013, 1
Wang, Q. D., et al. 2013, eprint arXiv:1307.5845

Yuan, F., Quataert, E., & Narayan, R. 2003, ApJ, 598, 301